International Journal of Heat and Fluid Flow 39 (2013) 78–89

Contents lists available at SciVerse ScienceDirect

International Journal of Heat and Fluid Flow

journal homepage: www.elsevier.com/locate/ijhff

Modeling rotation and curvature effects within scalar eddy viscosity model framework

Sunil K. Arolla *, Paul A. Durbin

Department of Aerospace Engineering, Iowa State University, Ames, IA 50011, USA

ARTICLE INFO

Article history:
Received 10 August 2012
Received in revised form 10 November 2012
Accepted 20 November 2012
Available online 3 January 2013

Keywords:
Eddy viscosity
Frame rotation
Streamline curvature
Curved homogeneous shear
Bifurcation diagram
Modified coefficients

ABSTRACT

Two approaches to incorporate the effects of rotation and curvature in scalar eddy viscosity models are explored. One is the "Modified coefficients approach" – to parameterize the model coefficients such that the growth rate of turbulent kinetic energy is suppressed or enhanced. The other is the "Bifurcation approach" – to parameterize the eddy viscosity coefficient such that the equilibrium solution bifurcates from healthy to decaying solution branches. Simple, yet, predictive models in each of these two approaches are proposed and validated on some benchmark test cases characterized by profound effects of system rotation and/or streamline curvature. The results obtained with both the models are encouraging.

1. Introduction

Scalar turbulence closure models are the workhorses of industrial CFD. But, their native formulation is insensitive to rotation and curvature. Second moment closures (SMC) can account for these effects in a systematic manner because of the presence of exact production terms containing mean flow gradients and system rotation. They also contain the convective transport of the second moments and hence provide an accurate means for predicting the curved flows. Explicit Algebraic Reynolds Stress Models (EARSM) also retain the exact production terms, but are not frame invariant. Invariant methods have been proposed by Girimaji (1997) using an acceleration based coordinate system and by Gatski and Jongen (2000) using a strain rate based coordinate system following the ideas of Spalart and Shur (1997). But, the SMCs and the EARSMs are still not tractable in complex industrial applications due to excessive computational cost and numerical stiffness. This is the motivation to incorporate rotation/curvature effects into the scalar, eddy viscosity framework.

Methods to sensitize scalar turbulence closure models to rotation and curvature can be categorized into the "Modified coefficients approach" and the "Bifurcation approach". A review of the machinery used in these approaches can be found in Durbin (2011).

The modified coefficients approach dates back to 1980. Howard et al. (1980) modified turbulence length scale by adding rotation dependent terms to the dissipation rate equation. Several others also have introduced ad hoc rotation/curvature dependent terms into the ε transport equation (see Cazalbou et al., 2005). Hellsten (1998) extended the work of Khodak and Hirsch (1996) by introducing parametric dependency into the destruction term of the specific dissipation rate equation. Spalart and Shur (1997) introduced a correction to the production term in a transport equation for eddy viscosity. They proposed a unified measure for rotation and curvature in terms of the material derivative of the strain rate tensor, making the model frame independent and Galilean invariant. More recently, Smirnov and Menter (2009) applied the Spalart–Shur correction to the SST variant of $k-\omega$ by correcting the production terms in both the TKE and the ω transport equations. A criticism of a model which corrects the production term in the TKE equation without a corresponding correction of the eddy viscosity in the momentum equation is that it violates energy conservation: energy extracted from the mean flow by the turbulence is not in balance with the production of turbulent kinetic energy.

Pettersson-Reif et al. (1999) proposed a novel approach to sensitize the scalar turbulence models to rotational effects. Bifurcation analysis of SMCs in rotating homogeneous shear flow forms the basis for this work. The model is formulated such that the equilibrium solution bifurcates from healthy to decaying solution branches. The original method was proposed in conjunction with the v^2-f model. In principle, it can be used with any scalar turbulence model, but prior to the present paper, that has not been

* Corresponding author.
E-mail addresses: asunil@iastate.edu (S.K. Arolla), durbin@iastate.edu (P.A. Durbin).

0142-727X/$ - see front matter © 2012 Elsevier Inc. All rights reserved.
http://dx.doi.org/10.1016/j.ijheatfluidflow.2012.11.006

pursued. Duraisamy and Iaccarino (2005) have extended this for curved flows and tested it on a tip vortex. Dhakal and Walters (2011) follow a similar approach, but they introduce an additional equation to tackle numerical convergence issues.

In this work, we follow the approach proposed by Pettersson-Reif et al. (1999) with an objective to simplify the functional form of the model while retaining the predictive capability. We perform the analysis of the proposed model for its bifurcation behavior in homogeneous curved shear flow and compare the salient points on the bifurcation diagram with that using the linearized SSG model. Based on the understanding gained from the bifurcation approach, we also propose a simple model to parameterize the production term in the ω transport equation. The two new models are tested on several cases in which rotation and curvature are known to have profound influence.

Since the modeling framework proposed in this work unifies rotation and curvature, we use the terminology "rotation correction" and "curvature correction" interchangeably throughout this paper.

2. Scalar eddy viscosity model framework

We use SST variant of $k-\omega$ (Menter, 1993) as the base turbulence model. But, in principle, the modeling framework developed herein can be used for any other scalar closure model.

2.1. SST variant of $k-\omega$ model

Stated briefly, the SST model is of the form

$$\frac{\partial k}{\partial t}+u_j\frac{\partial k}{\partial x_j}=\mathcal{P}-\varepsilon+\frac{\partial}{\partial x_j}\left[\left(\nu+\frac{\nu_T}{\sigma_k}\right)\frac{\partial k}{\partial x_j}\right] \tag{1}$$

where $\varepsilon=\beta^* k\omega$ and $\mathcal{P}=\nu_t\mathcal{S}^2$.

$$\frac{\partial \omega}{\partial t}+u_j\frac{\partial \omega}{\partial x_j}=\frac{\gamma}{\nu_T}\mathcal{P}-D_\omega+\frac{\partial}{\partial x_j}\left[\left(\nu+\frac{\nu_T}{\sigma_\omega}\right)\frac{\partial \omega}{\partial x_j}\right]+CD_\omega \tag{2}$$

where $D_\omega=\beta\omega^2$ and CD_ω is the cross-diffusion term. The eddy viscosity, with no accounting for curvature effects, is $\nu_T=C_\mu k/\omega$ with $C_\mu=1.0$.

2.2. Bifurcation approach

In homogeneous shear flow, the turbulent kinetic energy and dissipation rate evolve as

$$\frac{Dk}{Dt}=\mathcal{P}-\varepsilon;\quad \frac{D\varepsilon}{Dt}=\frac{C_{\varepsilon1}\mathcal{P}-C_{\varepsilon2}\varepsilon}{T} \tag{3}$$

Combining these equations results in the following evolution equation for the timescale ratio

$$\frac{D}{D(\mathcal{S}t)}\left(\frac{\varepsilon}{\mathcal{S}k}\right)=\left(\frac{\varepsilon}{\mathcal{S}k}\right)^2\left[(C_{\varepsilon1}-1)\mathcal{P}_\mathcal{R}-(C_{\varepsilon2}-1)\right] \tag{4}$$

where $\mathcal{P}_\mathcal{R}=\mathcal{P}/\varepsilon$.

This equation admits two equillibria by setting the left hand side to zero (Speziale and MacGiollaMhuiris, 1989). They are:

$$\mathcal{P}_\mathcal{R}=(C_{\varepsilon2}-1)/(C_{\varepsilon1}-1);\quad \left(\frac{\varepsilon}{\mathcal{S}k}\right)_\infty=0 \tag{5}$$

The point at which both these equilibrium solutions coexist is the bifurcation point. Durbin and Pettersson-Reif (1999) noted that SMC model bifurcation is not immediately a stabilizing bifurcation. Turbulence stabilization occurs past the bifurcation point at the so-called restabilization point where the ratio of turbulence production to dissipation rate is equal to 1.

The idea in this approach is to introduce a functional dependence into the eddy viscosity coefficient (C_μ) such that the model bifurcates. In rotating and convexly curved flows, the turbulence production decreases. If the rate of rotation or the convex curvature is strong enough, turbulence can no longer be sustained resulting in relaminarization. We use a functional dependency on C_μ to create this effect directly.

2.2.1. Pettersson-Reif et al. (1999) extended to SST $k-\omega$

Pettersson-Reif et al. (1999) introduce their model into the v^2-f turbulence model. We extend this to the $k-\omega$ model as $\nu_T=C^*_\mu k/\omega$. In Pettersson-Reif et al. (1999), the functional form for the rotation correction is given by:

$$C^*_\mu=\frac{1+\alpha_2|\eta_3|+\alpha_3\eta_3}{1+\alpha_4|\eta_3|}\left(\sqrt{\frac{1+\alpha_5\eta_1}{1+\alpha_5\eta_2}}+\alpha_1\sqrt{\eta_2}\sqrt{|\eta_3|-\eta_3}\right)^{-1} \tag{6}$$

where $\eta_1\equiv S^*_{ij}S^*_{ij}$; $\eta_2\equiv\Omega^*_{ij}\Omega^*_{ij}$ and $\eta_3\equiv\ \eta_1-\eta_2$. The model constants are: $\alpha_1=0.055$, $\alpha_2=0.5$, $\alpha_3=0.25$, $\alpha_4=0.2$, $\alpha_1=0.025$. Unlike Pettersson-Reif et al. (1999), we do not use damping functions. Also, C^*_μ is limited to a maximum value of 2.5.

2.2.2. Proposed new model

The functional form proposed by Pettersson-Reif et al. (1999) uses the bifurcation diagram of SMCs as a tool in guiding the model development. But, there is no evidence in the literature that suggests the models should behave exactly in the same way as SMCs as the parameter $\Omega^F/\mathcal{S}$ is varied. So, our idea in this work is to follow the same approach but enforce only the bifurcation and restabilization points to be close to SMCs. We do not enforce the SMCs behavior for the entire range of $\Omega^F/\mathcal{S}$. The following constraints are imposed on the functional form for a well-behaved model. The model should:

1. Retain the original form in the absence of curvature or rotation $\left(C^*_\mu=C_\mu\right)$.
2. Bifurcate between only two possible stable non-rotating solutions: $(\varepsilon/\mathcal{S}k)_\infty=0.208;(\varepsilon/\mathcal{S}k)_\infty=0$.
3. Yield restabilization close to $\Omega^F/\mathcal{S}=0\&0.5$ in rotating homogeneous shear flow.
4. Yield a maximum value of $(\varepsilon/\mathcal{S}k)$ close to $\Omega^F/\mathcal{S}=0.25$.
5. Behave as $C_\mu\approx\eta_1^{-1}$ as $\eta_1\ \to\infty$ so that $lim_{\eta_1\to\infty}C^*_\mu\eta_1$ is finite.
6. Behave as $C^*_\mu\approx1/\sqrt{\eta_1}$ when $\eta_1\gg\eta_2$.

Several functional forms have been tried and we selected the following:

$$C^*_\mu=C_\mu\left(\alpha_1(|\eta_3|-\eta_3)+\sqrt{1-min(\alpha_2\eta_3,0.99)}\right)^{-1} \tag{7}$$

To evaluate the model coefficients, we insert C^*_μ in the moving equilibrium solution: on branch 1,

$$\mathcal{P}/\varepsilon=(C_{\varepsilon2}-1)/(C_{\varepsilon1}-1) \tag{8}$$

For the $k-\varepsilon$ model, $\mathcal{P}=2\nu_t|S|^2\equiv\nu_t\mathcal{S}^2$ where ν_t is the eddy viscosity, $C^*_\mu k^2/\varepsilon$. Substitution into Eq. (8) gives

$$\left(\frac{\varepsilon}{\mathcal{S}k}\right)^2=C^*_\mu(C_{\varepsilon1}-1)/(C_{\varepsilon2}-1) \tag{9}$$

In parallel shear flow subjected to orthogonal mode rotation, the non-dimensional strain rate tensor is given by

$$S^*_{ij}=\frac{1}{2}\frac{\mathcal{S}k}{\varepsilon}\begin{pmatrix}0&1&0\\1&0&0\\0&0&0\end{pmatrix}$$

and the non-dimensional rotation rate tensor is given by

$$\Omega^*_{ij} = \frac{1}{2}\frac{\mathcal{S}k}{\varepsilon}\left(1 - 2C_r\frac{\Omega^F}{\mathcal{S}}\right)\begin{pmatrix}0 & -1 & 0\\ 1 & 0 & 0\\ 0 & 0 & 0\end{pmatrix}$$

The dimensionless velocity gradient invariants are

$$\begin{aligned}\eta_1 &\equiv S^*_{ij}S^*_{ij} = \frac{1}{2}(\mathcal{S}k/\varepsilon)^2\\ \eta_2 &\equiv \Omega^*_{ij}\Omega^*_{ij} = -\Omega^*_{ij}\Omega^*_{ji} = \frac{1}{2}(\mathcal{S}k/\varepsilon)^2\left(1 - 2C_r\frac{\Omega^F}{\mathcal{S}}\right)^2\\ \eta_3 &\equiv \eta_1 - \eta_2; \quad \mathfrak{R}^2 \equiv \frac{\eta_2}{\eta_1} = \left(1 - 2C_r\frac{\Omega^F}{\mathcal{S}}\right)^2\end{aligned} \tag{10}$$

$C_r = 2.0$ was found to give best agreement with the data for the test cases considered in this study.

After substituting Eqs. (7) and (9) becomes

$$\begin{aligned}&[\alpha_1(|1-\mathfrak{R}^2| - (1-\mathfrak{R}^2)) - 0.086086]^2\\ &= \frac{1}{\eta_1^2} - \frac{1}{\eta_1^2}min[\alpha_2\eta_1(1-\mathfrak{R}^2), 0.99]\end{aligned} \tag{11}$$

When plotted as $\varepsilon/\mathcal{S}k$ vs. $\Omega^F/\mathcal{S}$, this is branch 1 of the bifurcation diagram as shown in Fig. 1.

On branch 2, the solution is trivial $\varepsilon/\mathcal{S}k \equiv 1/\sqrt{2\eta_1} = 0$. In Fig. 1, the points where $\mathcal{P}_\mathcal{R} \equiv \mathcal{P}/\varepsilon$ crosses unity on the Y-axis give the restabilization points. The analysis starts with $\mathcal{P}_\mathcal{R}$, given by:

$$\mathcal{P}_\mathcal{R} = C^*_\mu(\mathcal{S}k/\varepsilon)^2 \tag{12}$$

Substituting for C^*_μ and taking the limit $\eta_1 \to \infty$,

$$\mathcal{P}_\mathcal{R} = \frac{2C_\mu}{\alpha_1[|1-\mathfrak{R}^2| - (1-\mathfrak{R}^2)]} \tag{13}$$

which is plotted as branch 2 on the bifurcation diagram (see Fig. 1). The model coefficients are tuned such that the bifurcation and restabilization points predicted by the proposed model are close to the SMCs. We selected $\alpha_1 = 0.04645$ and $\alpha_2 = 0.25$ and C^*_μ is limited to a maximum value of 2.5 (to avoid excessive turbulent diffusion). From Table 1, it can be concluded that the bifurcation and restabilization points predicted by both Pettersson-Reif et al. (1999) and the proposed new model are in close agreement with the linearized SSG model (see Appendix A.2 for bifurcation analysis of the linearized SSG model).

Now, let us consider curved homogeneous shear flow. It is a homogeneous idealization of a flow with circular streamlines (Holloway and Tavoularis, 1989). Homogeneity in a flow confined between inner and outer cylindrical walls can be sought in the limit of large radii and by assuming that the distance between the two walls is far greater than the turbulence length scales. Curved homogeneous shear flow is characterized by shear rate and curvature factor given by

$$\mathcal{S} = \frac{\partial U}{\partial r}, \quad \xi = \left(\frac{U_c}{R_c}\right)/\mathcal{S} \tag{14}$$

where the tangential velocity, $U = U_c + \mathcal{S}r$ with $\mathcal{S}$ being constants in homogeneous shear flow; R_c is the radius of curvature and r is the radial coordinate measured from the center of the curvature. $\xi > 0$ corresponds to convex curvature which is stabilizing, $\xi < 0$ corresponds to concave curvature which is destabilizing.

The non-dimensional strain rate tensor for this case is obtained by transforming to the streamline coordinate system and is given by

$$S^*_{ij} = \frac{1}{2}\frac{\mathcal{S}k}{\varepsilon}(1-\xi)\begin{pmatrix}0 & 1 & 0\\ 1 & 0 & 0\\ 0 & 0 & 0\end{pmatrix}$$

The non-dimensional rotation rate tensor is given by

$$\Omega^*_{ij} = \frac{1}{2}\frac{\mathcal{S}k}{\varepsilon}[1+\xi+2(C_r-1)\xi]\begin{pmatrix}0 & -1 & 0\\ 1 & 0 & 0\\ 0 & 0 & 0\end{pmatrix}$$

The dimensionless velocity gradient invariants are

$$\begin{aligned}\eta_1 &\equiv S^*_{ij}S^*_{ij} = \frac{1}{2}(\mathcal{S}k/\varepsilon)^2(1-\xi)^2\\ \eta_2 &\equiv \Omega^*_{ij}\Omega^*_{ij} = -\Omega^*_{ij}\Omega^*_{ji} = \frac{1}{2}(\mathcal{S}k/\varepsilon)^2[1+\xi+2(C_r-1)\xi]^2\\ \eta_3 &\equiv \eta_1 - \eta_2; \quad \mathfrak{R}^2 \equiv \frac{\eta_2}{\eta_1}\end{aligned} \tag{15}$$

As $\mathfrak{R}$ is now a function of ξ alone, the solution can be plotted as $\mathcal{P}_\mathcal{R}$ vs. ξ as shown in Fig. 1.

From Fig. 1, it can be observed that there is only one bifurcation point in curved homogeneous shear flow. The higher the value of C_r, the earlier the restabilization is. As shown in Table 2, the proposed model with $C_r = 2.0$ predicts the bifurcation and restabilization

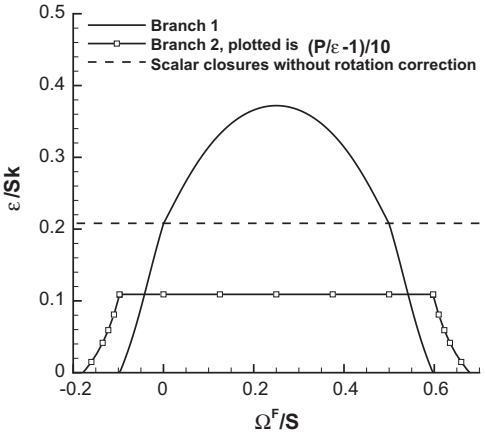

(a) Rotating homogeneous shear flow

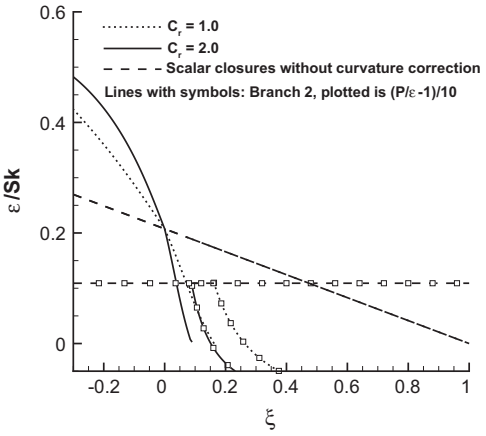

(b) Curved homogeneous shear flow: Note that the scalar closures without curvature correction cannot predict restabilization

Fig. 1. Bifurcation diagram in homogenous shear flow.

Table 1
Salient points on the bifurcation diagram: Rotating homogeneous shear flow.

Model	$(\Omega^F/S)_{bifurcation}$	$(\Omega^F/S)_{restabilization}$
Pettersson-Reif et al. (1999) (with $C_r = 2.25$)	(+0.522, −0.075)	(+0.6065, −0.162)
New model	(+0.597, −0.097)	(+0.678, −0.178)
linearized SSG	(+0.550, −0.1)	(+0.620, −0.17)

Table 2
Salient points on the bifurcation diagram: Curved homogeneous shear flow.

Model	$\xi_{bifurcation}$	$\xi_{restabilization}$
$C_r = 1.0$	0.162	0.263
$C_r = 2.0$	0.089	0.1515
Linearized SSG	0.1	0.15

points in close agreement with those predicted by the linearized SSG model (see Appendix A.2).

2.3. Modified coefficients approach

2.3.1. Proposed η_3 based model

With the understanding gained from the bifurcation approach, we propose a modified coefficient model for the production term of the ω-equation. Replace the first term on the right side of Eq. (2) by $P_\omega = \gamma F_{rc} \mathcal{S}^2$ where

$$F_{rc} = (1.0 + \alpha_1 |\eta_3| + 3\alpha_1 \eta_3) \tag{16}$$

In our previous work (Arolla and Durbin, 2012), we have tried correcting the destruction term of the TKE equation. Although, it did give good results in some benchmark test cases, it can interfere with the stress limiter and blending functions defined in the base turbulence model and hence can cause troubles in complex cases.

Since F_{rc} is not bounded, we impose an upper clip at 10.0 which was sufficiently high to cause the stabilization of turbulence and a lower clip at 0.0 to avoid negative dissipation. A value of $\alpha_1 = -0.2$ was found to be optimum for the cases tested here.

2.3.2. Br based model (Hellsten; Khodak & Hirsch)

We will compare to a model of Hellsten (1998). This model is motivated by the Bradshaw number $Br = Ro(Ro + 1)$ where $Ro \equiv -2\Omega^F/\partial_y U$. Khodak and Hirsch (1996) suggest replacing frame rotation in the Bradshaw number by $|\mathbf{\Omega}^A| - |\mathbf{S}|$. Hellsten (1998) uses $D_\omega = F_4 \beta \omega^2$ for the destruction term in the ω-equation with

$$F_4 = \frac{1}{1 + C_{RC} Br} \tag{17}$$

where $Br = \sqrt{\frac{\eta_2}{\eta_1}}\left(\sqrt{\frac{\eta_2}{\eta_1}} - 1\right)$. The model constants are: $C_{RC} = 3.6$ and $C_r = 1.0$.

2.4. Unification of rotation and curvature

Rotation and curvature are analogous. Analysis of SMCs to understand this analogy is outlined in Appendix A.1. For turbulence closure modeling, rotation and curvature can be unified using Spalart–Shur tensor as discussed in Durbin (2011). The definitions of the rate of strain and rate of rotation are given by:

$$S_{ij} = \frac{1}{2}(\partial_j U_i + \partial_i U_j); \quad \Omega^{mod}_{ij} = \Omega^A_{ij} + (C_r - 1) W^A_{ij} \tag{18}$$

where $\Omega^A_{ij} = \Omega^{rel}_{ij} + \Omega^F_{ij}$ with $\Omega^{rel}_{ij} = \frac{1}{2}(\partial_i U_j - \partial_j U_i)$ and $\Omega^F_{ij} = -\epsilon_{ijk}\Omega^F_k$. Ω^F_k is the angular frame velocity about the x_k-axis. The Spalart–Shur tensor is defined in terms of the strain rate tensor as:

$$\mathbf{\Omega}^{SS} \equiv \mathbf{\Omega}^F - \frac{\mathbf{S}.D_t\mathbf{S} - D_t\mathbf{S}.\mathbf{S}}{2|\mathbf{S}|^2} \tag{19}$$

In 2D, $W^A_{ij} = \Omega^{SS}_{ij}$. In 3D, this is changed to $W^A_{jk} = \Omega^F_{jk} - \epsilon_{ijk} w_i$ in which

$$w_i = II_S X_{ij}\left(\Omega^F_{pq}\epsilon_{pqj} - \Omega^{SS}_{rs}\epsilon_{rsj}\right)$$

$$X_{ij} = \frac{II_S^2\delta_{ij} + 12III_S S_{ij} + 6II_S S_{ik}S_{kj}}{2II_S^3 - 12III_S^2}$$

where $II_S = S_{ij}S_{ji}$ and $III_S = S_{ij}S_{jk}S_{ki}$.

The invariants used in the models are

$$\eta_1 = S_{ij}S_{ij}T^2; \quad \eta_2 = \Omega^{mod}_{ij}\Omega^{mod}_{ij}T^2; \quad \eta_3 = \eta_1 - \eta_2$$

The coefficient C_r takes a value of 2 for the bifurcation approach and for the η_3 based model. For the Br based model, $C_r = 1$. This means that the Br based model does not use the Spalart–Shur tensor. The numerical implementation of the models is discussed elsewhere (Arolla and Durbin, in preparation).

2.5. Numerical issues

For the test cases studied in this work, the numerical convergence with the models from the modified coefficients approach has been observed to be consistently better than that with the models from the bifurcation approach. Dhakal and Walters (2011) propose to use an additional transport equation to get numerically convergent solutions. Instead, we use a small under-relaxation on η_2 as follows:

$$\eta_2^{new} = (1 - \alpha_u)\eta_2^{old} + \alpha_u \Omega^{mod}_{ij}\Omega^{mod}_{ij}T^2 \tag{20}$$

The under-relaxation factor, $\alpha_u = 0.1$ was used for all the test cases. Another approach is to under-relax the eddy viscosity itself.

The usual definition of timescale used in Eq. (20) is

$$T = max\left(\frac{1}{\beta^*\omega}, 6\sqrt{\frac{\nu}{\beta^* k\omega}}\right) \tag{21}$$

This is singular at the wall. The TKE in the $k-\omega$ model behaves as $y^{3.23}$ near a solid wall and ω behaves as $1/y^2$ (Kalitzin et al., 2005). Hence the second term in (20) goes as $1/y^{0.625}$ which is singular at $y = 0$. For a better near-wall behavior, we use $T = max(T_1, T_3)$ where

$$T_1 = \frac{1}{\beta^*\omega}; \quad T_2 = 6\sqrt{\frac{\nu}{\beta^* k\omega}}; \quad T_3 = \left(T_1^n T_2\right)^{1/n+1} \tag{22}$$

with $n = 1.625$ to get $T \propto y$ near the wall.

3. Results and discussion

Test cases are chosen in which the effect of rotation and curvature enter the mean flow predominantly through the changes in turbulent stresses. Detailed comparison of both the mean velocity and the skin friction is made with the data from experiments or DNS. Unless otherwise mentioned explicitly, we have used OpenFOAM for all the computations discussed in this section.

3.1. Rotating plane channel

The flow physics in spanwise rotating channel flow have been studied in a number of experiments and numerical simulations (Johnston et al., 1972; Kristoffersen and Andersson, 1993; Grundestam et al., 2008). For fully developed flow, invoking the parallel flow assumption that U is a function only of y and with an angular velocity, Ω^F, about the spanwise z-axis, the mean U-momentum equation simplifies to

$$0 = -\frac{\partial P^*}{\partial x} + \frac{\partial}{\partial y}\left((\nu + \nu_t)\frac{\partial U}{\partial y}\right) \tag{23}$$

where P^* is the effective pressure with the centrifugal force absorbed. The effect of rotation enters the mean flow field only indirectly through the changes in the turbulent stresses modeled in ν_t. The imposed rotation breaks the symmetry of the flow field causing stabilization of the turbulence on one side and destabilization on the other side.

The flow conditions for this test case are consistent with the DNS of Kristoffersen and Andersson (1993): $Re_\tau \equiv u_\tau h/\nu = 194$ where h is the channel half-width. The $k-\omega$ model, by design, predicts the near-wall turbulent kinetic energy peak incorrectly. And hence, we limit our comparisons to the mean velocity and skin friction.

Fig. 2 compares the mean velocity profiles predicted by curvature models with the DNS data of Kristoffersen and Andersson (1993) and Grundestam et al. (2008). The results show excellent agreement with the DNS data. On the "stable" side of the channel, the frame rotation is in the direction opposite to the background shear; hence, the eddy viscosity is reduced due to the suppression of turbulence. This reduces the resistance to the flow thereby increasing the velocity. On the "unstable" side, the eddy viscosity is increased due to enhancement of turbulence, resulting in lower velocity. This explains the asymmetry of the velocity profiles in Fig. 2. An irrotational core region is observed at the center of the channel where $dU/dy = 2\Omega^F$. It is in agreement with the linear stability theory – the irrotational core region corresponds to neutral stability.

At Ro = 0.1, all the rotation correction models agree well with the DNS data. At high rotation numbers, the *Br* based model fails to respond adequately. Pettersson-Reif et al. (1999) and both the proposed models show good agreement. As the rotation rate increases, the flow tends to relaminarize. The velocity profiles tend towards parabolic, as shown in Fig. 2. The skin friction decreases allowing higher bulk velocities. This trend is captured very well by the proposed models as shown in Fig. 3. The normalized friction velocity trend with increasing Rotation numbers is also in good agreement with the DNS data. We predict complete relaminarization at Ro = 2.5 – a bit earlier than that observed by Grundestam et al. The skin friction loop is unclosed for the *Br* based model even at *Ro* = 3.0, which means that relaminarization occurs at much higher rotation numbers with this model. With reference to Figs. 1 and 2 of Smirnov and Menter (2009), the proposed models in this paper are as accurate as the Spalart–Shur correction to the SST $k-\omega$ model.

To understand where the rotation effects appear inside the boundary layer, the rotation correction factor is plotted as a function of wall distance normalized with friction velocity, $y^+ = yu_\tau/\nu$ for *Ro* = 0.1 in Fig. 5. A bifurcation based model is used and hence, $C^*_\mu > 1.0$ signifies the unstable side and $C^*_\mu < 1.0$ signifies the stable side. We find that the model is active immediately outside the viscous sub-layer. The dominant effect occurs around $y^+ \approx 30$. At a higher rotation number of *Ro* = 0.5, however, the rotation effect appears immediately close to the wall on the stable side and the recovery is much slower into the center of the channel compared to that at a low Rotation number. At *Ro* = 0.1, the recovery of the destabilizing effect is slower than of the stabilizing effect.

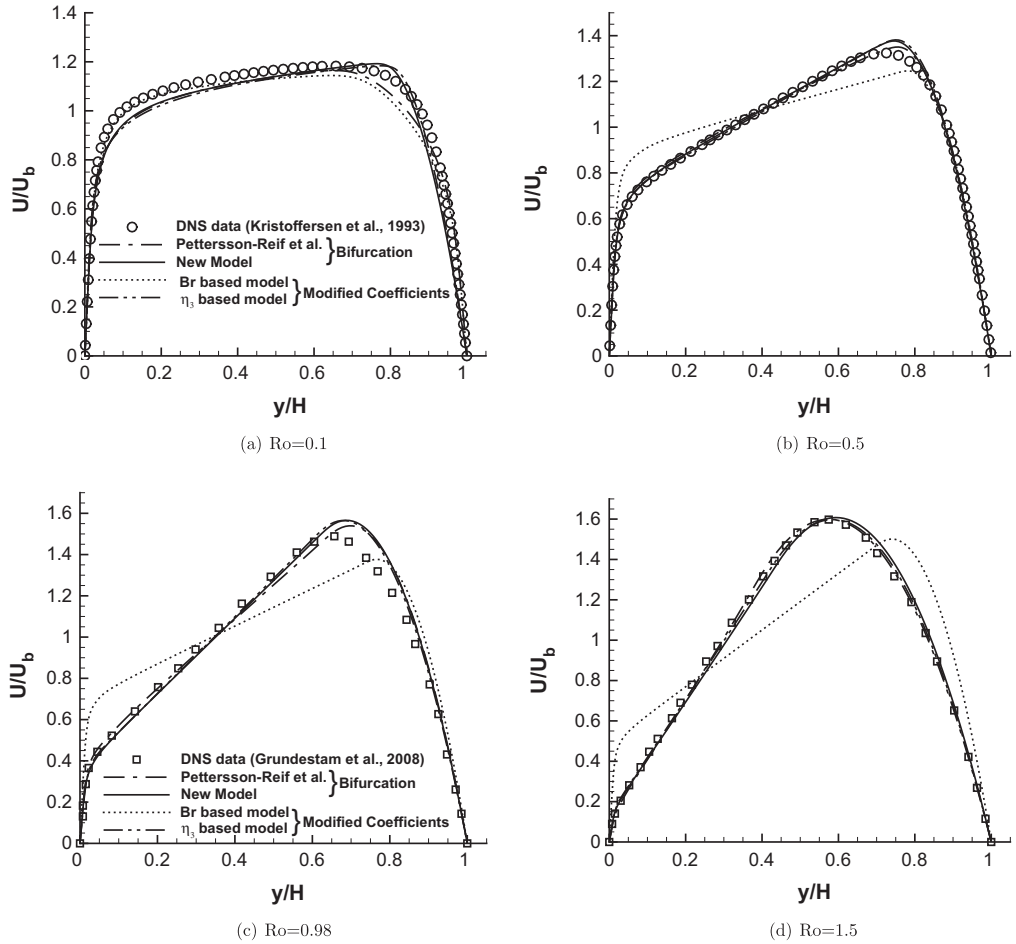

(a) Ro=0.1 (b) Ro=0.5

(c) Ro=0.98 (d) Ro=1.5

Fig. 2. Comparison of mean velocity profiles at different rotation numbers.

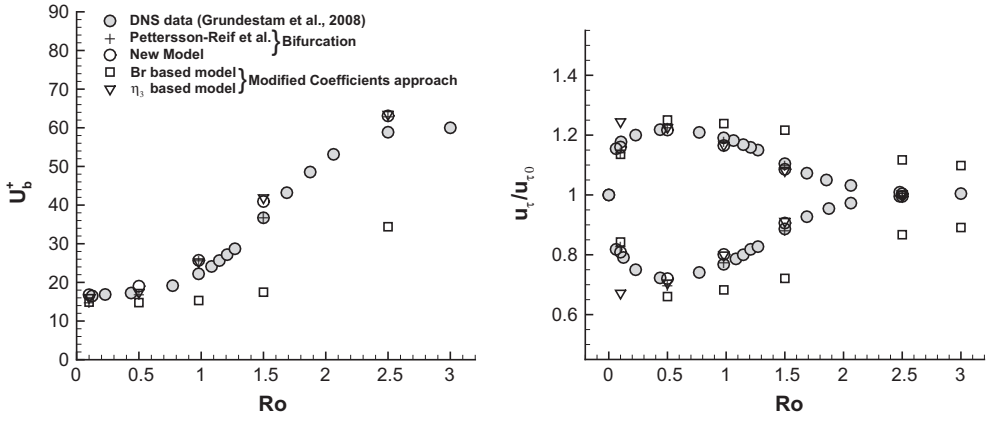

(a) Normalized bulk velocity (b) Normalized friction velocity

Fig. 3. Rotating channel flow: effect of rotation on bulk velocity and friction velocity.

3.2. Curved wall boundary layer

In analogy with rotation, streamline curvature can have profound influence on the flow field. Convex curvature suppresses the turbulence whereas concave curvature enhances it. In the case of convex curvature, the flow rotation is in the same direction as the rotation of the velocity vectors. For concave curvature, the two directions are opposite. Co-rotation stabilizes the turbulence, counter-rotation enhances it (Durbin, 2011). When the turbulence is suppressed, there will be less mean momentum transport from the freestream to the surface of the wall. Hence, wall shear decreases significantly and the tendency for the flow to separate increases. When the turbulence is enhanced, wall shear increases because of the increased turbulent mixing.

The governing equations for the mean flow in local plane polar coordinates, invoking the boundary-layer approximation are (Durbin, 1993)

$$\frac{U}{\alpha}\frac{\partial U}{\partial x}+V\frac{\partial U}{\partial y}=-\frac{1}{\alpha}\frac{\partial P}{\partial x}+\nu\frac{\partial^2 U}{\partial y^2}-\frac{\partial \overline{uv}}{\partial y}-\frac{2\overline{uv}}{\alpha R_c}$$
$$\frac{U^2}{\alpha R_c}=\frac{\partial (P+2k/3)}{\partial y};\quad \frac{\partial U}{\partial x}+\frac{\partial \alpha V}{\partial y}=0 \tag{24}$$

where $\alpha = 1 + y/R_c$ and $\overline{uv} = -\nu_t[\partial_y U - U/(\alpha R_c)]$. Here x denotes a direction parallel to the surface and U is the mean velocity in the x-direction; y denotes a direction normal to the boundary surface and V is the mean velocity in the y-direction. R_c is the radius of curvature of the surface and δ is the 99% boundary layer thickness. The above equations are solved by a spatial marching technique. $R_c/\delta = \infty$ for a flat plate boundary layer, $R_c/\delta > 0$ for convex wall and $R_c/\delta < 0$ for concave wall. Abrupt changes of surface curvature cause discontinuities, but the effect dies away quickly (Durbin, 1993). At the wall, a no-slip boundary condition is imposed with specific dissipation rate $\omega = 60\nu/[\beta(\Delta y)^2]$. At the freestream, $\partial_y U = -1/(\alpha R_c)$, $k = 10^{-5}U_\infty^2$ are imposed. For specific dissipation rate at the freestream (Menter, 1992)

$$\omega = \frac{4}{\beta^*}\frac{u_\tau^2}{U_{freestream}\delta^*} \tag{25}$$

3.2.1. Convex

Curvature is always associated with pressure gradients. To assess the curvature corrections, we use experiments of Gillis et al. (1980) and Simon et al. (1982) in which curvature effects are isolated by maintaining zero surface pressure gradient on the test wall. This was achieved by contouring the outer wall appropriately. The experimental set-up consists of a developing flat plate boundary layer which enters, at $Re_\theta = 4200$, a 90° constant-curvature bend with $\delta_{99}/R_c = 0.1$. Gillis et al. inferred the skin friction from the velocity measurements. But, we also compare with Simon et al. who measured the heat transfer coefficient, invoking Reynold's analogy.

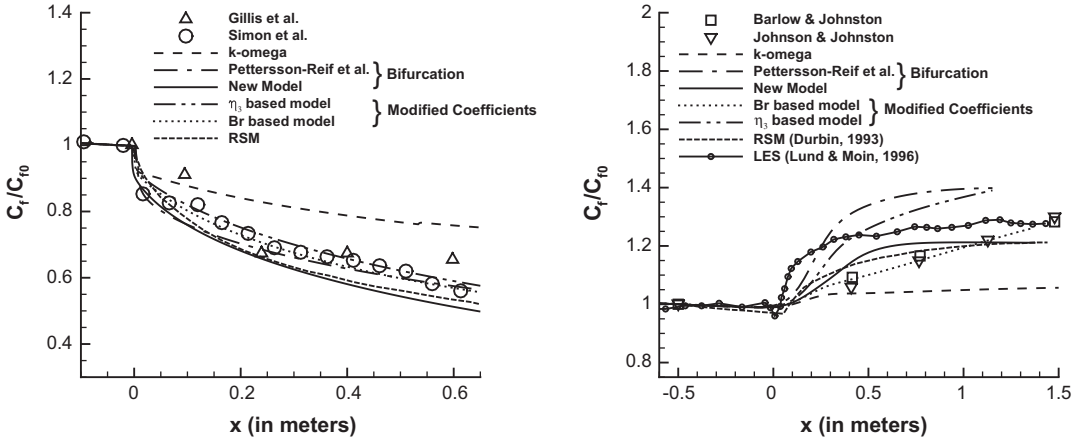

(a) Convex wall boundary layer (b) Concave wall boundary layer

Fig. 4. Skin friction plotted along the curved walls.

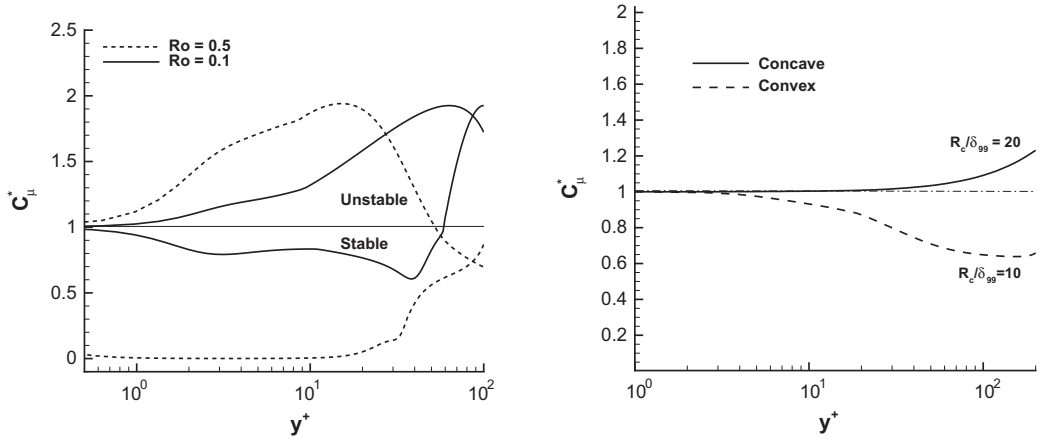

(a) Rotating Channel (b) Curved wall boundary layers

Fig. 5. Variation of rotation/curvature correction factors inside the boundary layer.

Fig. 4 compares the different curvature models with the experimental data and with an SMC model (Durbin, 1993). The $k-\omega$ model without curvature corrections underpredicts the effects of curvature. When a curvature correction is added, agreement with the data is improved.

3.2.2. Concave

Johnson and Johnston (1989) and Barlow and Johnston (1988) studied the effect of concave curvature on turbulence using a free-surface water channel. Similar to the Gillis et al., the pressure over the concave surface is maintained constant. The flow enters

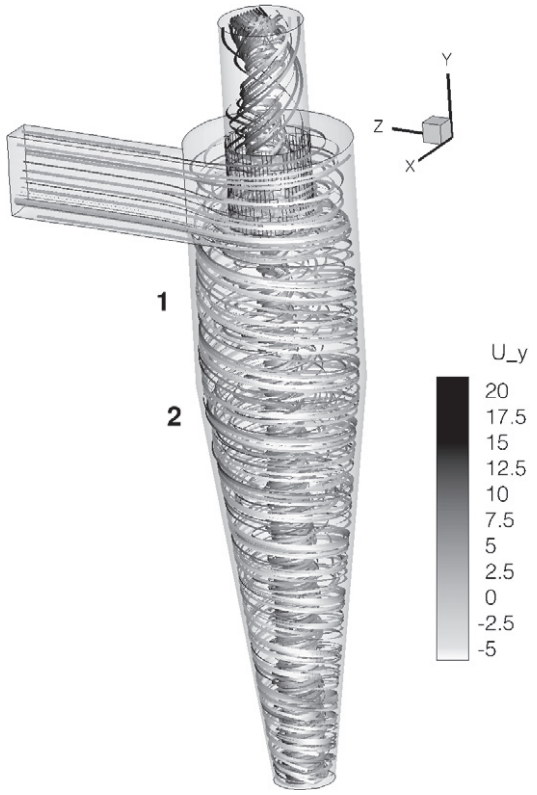

(a) Volume ribbons showing strongly swirling flow in Hydrocyclone. Ribbons are colored by axial velocity.

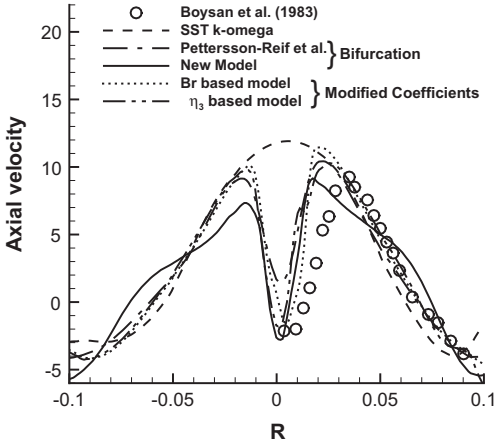

(b) Station1

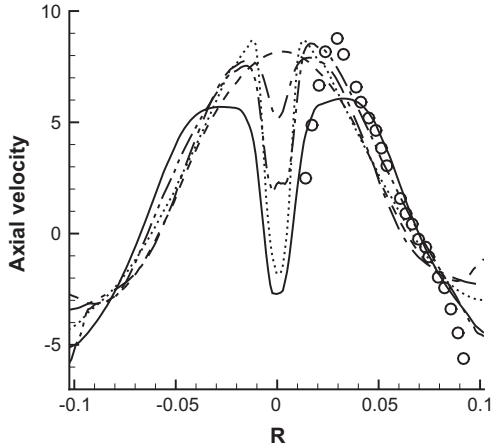

(c) Station2

Fig. 6. Hydrocyclone: axial velocity profiles at two different stations indicated on the left.

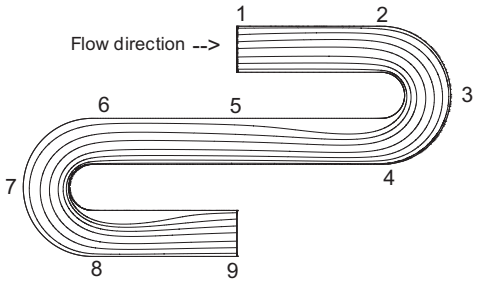

Fig. 7. Flow configuration of serpentine channel.

the curved section at $Re_\theta = 1140$ and the bend has a curvature of $\delta_{99}/R_c = 0.05$. Fig. 4 shows the comparison of the model predictions with the experimental data. The influence on the velocity profile is small. But, the skin friction increases significantly from the flat plate value. The skin friction data are inferred from the velocity profiles using a Clauser chart; but, LES of Lund and Moin (1996) suggest that the Clauser method could be in error. We also plotted their LES data. Qualitatively, the curvature models showed correct behavior for concave curvature.

To understand where the curvature effects are predominant inside the boundary layer, we plotted the curvature correction factor in Fig. 5 for the bifurcation based model. The models are active for $y^+ > 10$. The dominant effect occurs for $y^+ > 30$ for both concave and convex curvatures. This is consistent with observations in the rotating channel flow.

3.3. Hydrocyclone

Flow through a hydrocyclone is characterized by strongly swirling motion as shown in Fig. 6. Swirl induced suppression of turbulence results in a downward flow near the axis of the hydrocyclone. This cannot be predicted by the scalar eddy viscosity closures. Predicting downward flow is critical in the design of Hydrocyclones as it determines the separation efficiency of these devices.

We use a typical high-efficiency cyclone design of Stairmand, with a diameter of 0.205 m. Experimental data are from Boysan et al. (1983). The steady Navier–Stokes equations are solved using an incompressible solver in OpenFOAM. The cyclone inlet velocity corresponds to the volumetric flow rate of 0.08 $m^3\ s^{-1}$ (Slack et al., 2000). At the outflow, atmospheric pressure is specified. The bottom is closed.

The flow enters the hydrocyclone tangentially at the inlet. The vortex that is created undergoes stretching due to the contraction and hits the closed bottom, then reverses it's direction towards the vortex finder at the top. Due to the swirl, a low-pressure core forms at the center of the hydrocyclone allowing a downward flowing stream near the axis. Hence, the axial velocity contains zones of upward and downward flow. Rayleigh's centrifugal stability criterion explains the physics behind the effect of swirl in the vortex core (Durbin and Medic, 2007). From radial equilibrium,

$$\frac{\partial p}{\partial r} = \frac{u_\theta^2}{r} = \frac{L^2}{r^3} \tag{26}$$

where v_θ is the tangential velocity and $L = rv_\theta$ is the angular momentum. The stability criterion is that if $\partial\ L^2/\partial r > 0$, the flow is stable. The tangential injection of the flow ensures that this criterion is satisfied. And hence, turbulence is suppressed providing a path of low resistance for the downward stream.

The RANS simulations are carried out with different curvature models and the axial velocity at two different stations along the axis of hydrocyclone are compared with the experimental data in Fig. 6. The original SST $k-\omega$ model could not predict the downward flow at the core. All the curvature corrections show significant improvement over the original model.

3.4. Serpentine channel

The serpentine channel has both convex and concave curvatures (see Fig. 7) and when subjected to spanwise rotation, the separation bubble in the bends 1 and 2 differ. Recent DNS data from Laskowski and Durbin (2007) is used for comparison. The Reynolds number is $Re = 2\delta U_b/\nu = 5600$ where δ is the channel half-width. The curvature of the bend is $R_c/\delta = 2.0$. These simulations are attractive for their streamwise periodic inflow boundary conditions. Experimental data available for similar test cases require specification of accurate inflow boundary conditions consistent with the experimental set-up which is challenging. Periodicity between exit and inflow is invoked for the velocity, as in the DNS. In this work, we limit our investigation to the stationary case.

The key difference between the Serpentine channel and the curved wall boundary layers is that the effect of pressure gradient is present in the former, in addition to the effect of curvature. In analogy with flow over a cylinder, the flow accelerates over the first half of the inner curved wall (convex) and decelerates over the second half. On the outer curved wall (concave), the flow decelerates over the first half and accelerates in the second half. The

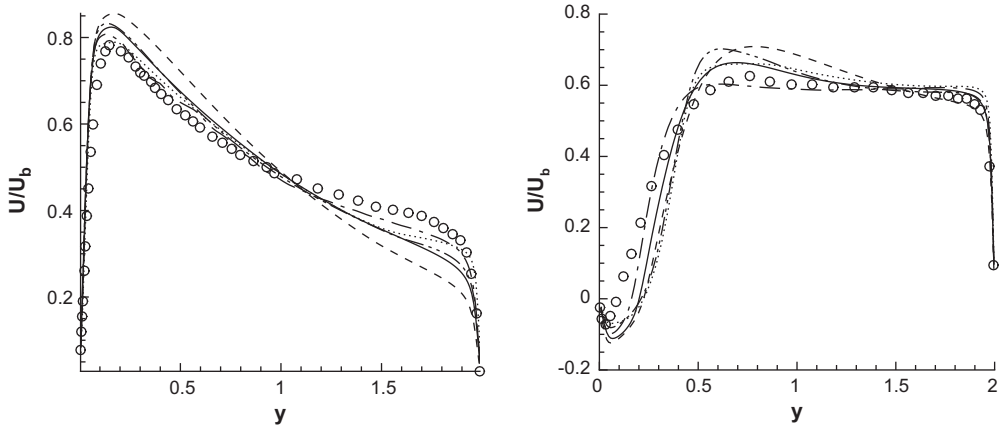

(a) Stations 3,7 (b) Stations 4,8

Fig. 8. Serpentine Channel, stationary: comparison of mean velocity profiles with Laskowski and Durbin (2007) data. For the legend, see Fig. 10.

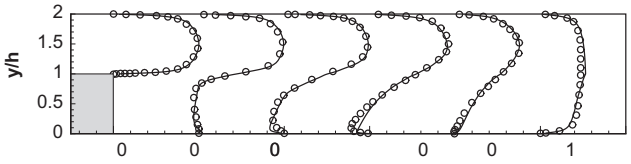

(a) Comparison of Mean velocity profiles with DNS of Barri and Andersson (2010)

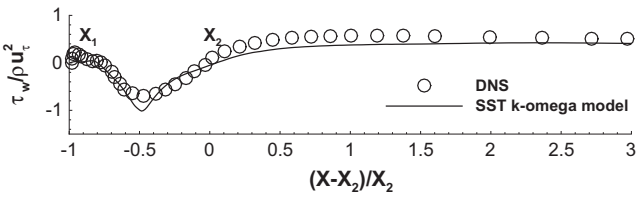

(b) Comparison of skin friction coefficient

Fig. 9. Backward-facing step, non-rotating case.

deceleration results in adverse pressure gradients and the flow is susceptible for separation. On the convex wall, the turbulence levels are suppressed and hence the flow cannot sustain the adverse pressure gradients and separates in the later half of the bend.

The mean velocity profiles at two different stations for the stationary case are plotted in Fig. 8 show that all the curvature corrections predict similar flow features. Pettersson-Reif et al. (1999) gives slightly better agreement compared to other models.

3.5. Rotating backward-facing step

The rotating backstep is a configuration which brings out the effect of spanwise rotation on the separation and reattachment of the free-shear layer downstream of the step. If the rotation is in the direction of mean shear, the turbulent mixing is enhanced and the size of the recirculation bubble is decreased. If the rotation is anti-parallel to the direction of mean shear, the turbulent mixing is suppressed and the size of the recirculation bubble increases. We use recent DNS data of Barri and Andersson (2010) at $Re = U_b(-H-h)/\nu = 5600$ to assess the rotation corrections on this complex flow configuration. The expansion ratio is $ER = H/(H-h) = 2$ with h being the step height and H being the downstream height of the channel. Following the DNS set-up, the spanwise rotation is imposed such that the turbulence over the stepped wall is enhanced and that over the opposite wall is suppressed.

A recycling inflow boundary condition is used so that fully developed turbulent conditions can be achieved upstream of the step. At the outflow, a pressure gradient in the wall-normal direction is imposed to balance the Coriolis force:

$$\frac{\partial P}{\partial y} \approx -2\Omega^F U \tag{27}$$

The definition of rotation number is, $Ro = \Omega^F(H-h)/U_{b0}$. U_{b0} is the bulk velocity upstream of the step in the non-rotating case. However, note that the local rotation number in the downstream part of the channel is *4* times greater than upstream because the bulk velocity, U_b, downstream of the step is related to that upstream by $U_{b0}(H-h)/H$. Hence, the effect of rotation is much stronger downstream of the step.

In a backstep, the free-shear layer emanating from the step undergoes geometry-induced separation. When subjected to rotation, the turbulence on this wall is amplified. Due to enhanced turbulence levels, higher momentum fluid away from the wall is transported towards the wall. This shortens the reattachment length.

Fig. 9 presents mean flow results for the non-rotating case using the SST $k-\omega$ turbulence model. From the mean velocity profiles, it can be observed that the flow reattaches earlier than that predicted by DNS. This is consistent with the skin friction prediction as well. Moreover, post-reattachment the skin friction is not in good agreement with the data. Hence, when evaluating the effectiveness of the proposed rotation corrections, it is important to understand that some discrepancies come from the base turbulence model itself and not the rotation correction per se.

Figs. 10–13 show the mean velocity profiles and the skin friction variation along the stepped wall at two rotation numbers. The proposed models show good agreement with the data up to the reattachment location. Post reattachment, the agreement is poor. At moderately high rotation numbers, DNS data show a separation bubble on the upper wall, opposite to the step. This is due to the stabilizing effect of rotation on that wall. The turbulence is suppressed on this surface and hence the flow is susceptible to separation. Both of the bifurcation models show separation even at low rotation numbers which is not seen in the DNS data. This was not the case when these corrections were used in conjunction with v^2-f model which predicts the correct level of turbulent

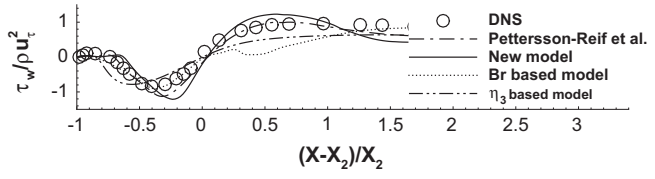

Fig. 10. Backward-facing step, Ro = 0.05: comparison of skin friction coefficient.

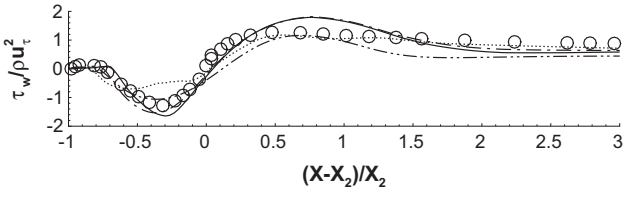

Fig. 12. Backward-facing step, Ro = 0.2: comparison of skin friction coefficient at Ro = 0.2. For the legend, see Fig. 10.

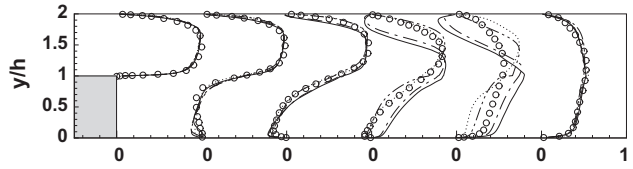

Fig. 11. Comparison of mean velocity profiles at Ro = 0.05.

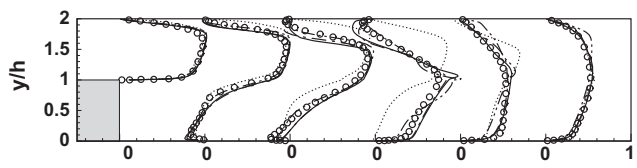

Fig. 13. Comparison of mean velocity profiles at Ro = 0.2.

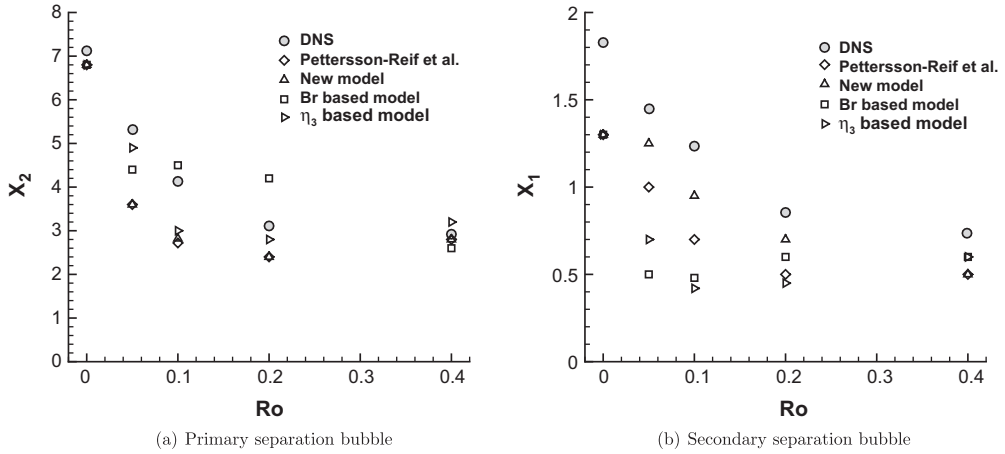

(a) Primary separation bubble (b) Secondary separation bubble

Fig. 14. Reattachment length plotted as a function of rotation number. For X_1 and X_2, see Fig. 9.

kinetic energy near the walls (Pettersson-Reif et al., 1999). This could be due to low Reynolds numbers used for the simulation and since using a turbulence model is not appropriate where the flow is laminar. Hence, we focus on the effect of rotation on the free shear layer emanating from the step.

The variation of the reattachment length of both the primary (X_2) and the secondary (X_1) separation bubbles with rotation number is plotted in Fig. 14. Both of the models from the bifurcation approach and η_3 based model predict the reattachment length more accurately than the *Br* based model. A trend of approximately constant reattachment length after $Ro = 0.2$ is captured very well by the models.

4. Concluding remarks

Simple models for rotation and curvature effects were proposed based on bifurcation analysis in rotating homogeneous shear flow. They are parameterized as a function of η_3. Extensive validation has been carried out to test the proposed models and to compare the bifurcation approach and the modified coefficients approach. The results obtained using these models are encouraging in all the test cases.

The η_3 based model proposed in the modified coefficients approach is competitive with the bifurcation based models in all the cases tested. In the rotating channel and rotating backstep cases, it performs better than *Br* based model proposed by Hellsten in responding appropriately to the imposed system rotation.

The derivation of the new model in the bifurcation approach is guided by the equilibrium analysis and hence can be thought of as a "physics based" model which is more reliable for use in the industrial design process.

Appendix A. Analysis of the second moment closures

A.1. Analogy between rotation and curvature

The evolution equation for the Reynolds stress anisotropy tensor in a rotating frame of reference is given by (Durbin and Pettersson-Reif, 2010):

$$\frac{k}{\varepsilon}d_t a_{ij} = (1-C_1)a_{ij} - a_{ij}\mathcal{P}_{\mathcal{R}} - (4/3-C_s)S^*_{ij} \times \underbrace{-a_{ik}S^*_{kj} - a_{jk}S^*_{ki} + 2/3\delta_{ij}a_{kl}S^*_{lk} - a_{ik}\Omega^*_{kj} - a_{jk}\Omega^*_{ki}}_{\Pi_{\text{rotation/curvature}}} \tag{A.1}$$

where

$$\begin{aligned} a_{ij} &= (1-C_2-C_3)[\overline{u_iu_j}/k - (2/3)\delta_{ij}] \\ S^*_{ij} &= [(1-C_2-C_3)S_{ij}]\frac{k}{\varepsilon} \\ \Omega^*_{ij} &= \left[(1-C_2+C_3)\Omega^A_{ij} + \epsilon_{ijl}\Omega^F_l\right]\frac{k}{\varepsilon} \end{aligned} \tag{A.2}$$

and the rate of production due to mean flow gradients and rotation/curvature is

$$\begin{aligned} \mathcal{P}_{ij} &= -\overline{u_iu_k}\left(S_{kj}+\Omega^A_{kj}\right) - \overline{u_ju_k}\left(S_{ki}+\Omega^A_{ki}\right) \\ \mathcal{P}_{\mathcal{R}} &= \mathcal{P}/\varepsilon; \quad \mathcal{P} = \mathcal{P}_{kk}/2 \end{aligned} \tag{A.3}$$

with the strain rate tensor and the absolute rotation tensor defined as

$$\begin{aligned} S_{ij} &\equiv 1/2(\partial_i U_j + \partial_j U_i) \\ \Omega^A_{ij} &\equiv 1/2(\partial_i U_j - \partial_j U_i) + \varepsilon_{ijk}\Omega^F_k \end{aligned} \tag{A.4}$$

where Ω^F_k is the angular frame velocity about x_k-axis. This will be denoted by Ω^F.

The constants for the linearized SSG model are: $C_2 = 0.4125$, $C_3 = 0.2125$, $C_s = 0.1844$ and $C_1 = 3.4$. The standard $k-\varepsilon$ model equations are used to complete the closure at this level.

In parallel shear flow subjected to orthogonal mode rotation, the non-dimensional strain rate tensor is given by

$$S^*_{ij} = \frac{1}{2}C_{S^*}\frac{\mathcal{S}k}{\varepsilon}\begin{pmatrix} 0 & 1 & 0 \\ 1 & 0 & 0 \\ 0 & 0 & 0 \end{pmatrix}$$

and the non-dimensional rotation rate tensor is given by

$$\Omega^*_{ij} = \frac{1}{2}C_{\Omega^*}\frac{\mathcal{S}k}{\varepsilon}\left(1-2C_r\frac{\Omega^F}{\mathcal{S}}\right)\begin{pmatrix} 0 & -1 & 0 \\ 1 & 0 & 0 \\ 0 & 0 & 0 \end{pmatrix}$$

where

$C_r = (2-C_2+C_3)/(1-C_2+C_3) = 2.25, C_{S^*} = (1-C_2-C_3) = 0.375$ and $C_{\Omega^*} = (1-C_2+C_3) = 0.8$ for the pressure-strain model considered.

It can be observed from Eq. (A.1) that frame rotation enters the evolution equation only through the last two of the underbraced terms. They contain contributions from both flow rotation and coordinate frame rotation. By substituting non-dimensional strain rate and rotation rate, the rate of production of the Reynolds shear stress anisotropy becomes:

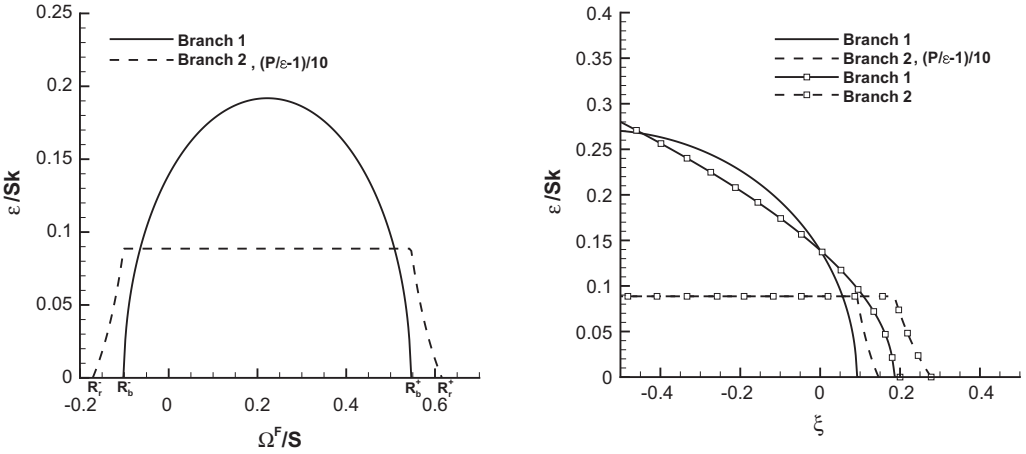

(a) Rotating homogeneous shear flow

(b) Curved homogeneous shear flow: Lines with symbols are for the case with the convective transport neglected

Fig. A.15. Bifurcation diagram for homogeneous shear flows.

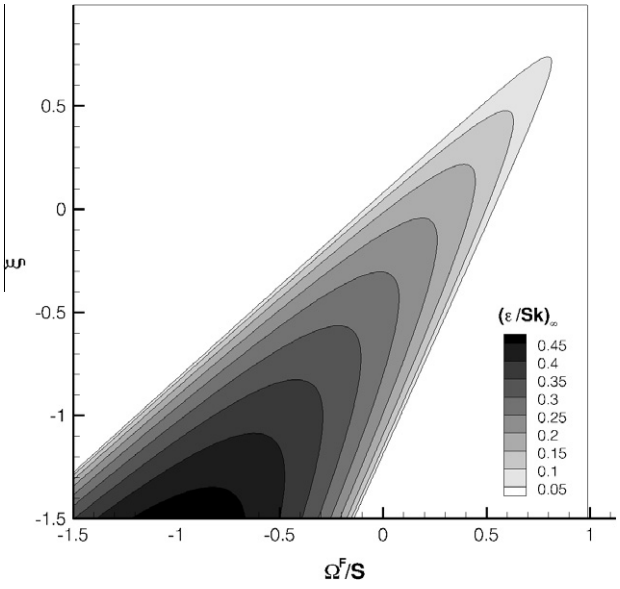

Fig. A.16. Bifurcation surface: Branch 1 solution. Bright region shows imaginary solution which is not physical.

$$\Pi_{12(rotation)} = \frac{\mathcal{S}k}{\varepsilon}\left[[a_{11}C_3 - a_{22}(1-C_2)] - \frac{\Omega^F}{\mathcal{S}}(2 - C_2 + C_3)(a_{11} - a_{22})\right] \tag{A.5}$$

Consider a case with $\mathcal{S} > 0$ and a positive imposed rotation, $\Omega^F > 0$. Usually, $a_{11} > a_{22}$ in parallel shear flow. Hence, Eq. (A.5) shows that frame rotation decreases the rate of production of the Reynolds shear stress anisotropy. This means that the magnitude of shear stress production is increased, since $\overline{uv}$ is negative in parallel shear flows. Negative rotation has the opposite effect.

In curved homogeneous shear flow, the non-dimensional strain rate tensor is given by

$$S^*_{ij} = \frac{1}{2}C_{\mathcal{S}^*}\frac{\mathcal{S}k}{\varepsilon}(1-\xi)\begin{pmatrix} 0 & 1 & 0 \\ 1 & 0 & 0 \\ 0 & 0 & 0 \end{pmatrix}$$

The non-dimensional rotation rate tensor is

$$\Omega^*_{ij} = \frac{1}{2}C_{\Omega^*}\frac{\mathcal{S}k}{\varepsilon}[1 + \xi + 2(C_r - 1)\xi]\begin{pmatrix} 0 & -1 & 0 \\ 1 & 0 & 0 \\ 0 & 0 & 0 \end{pmatrix}$$

By substituting non-dimensional strain rate and rotation rate tensor components into the underbraced terms of Eq. (A.1), the rate of production of the Reynolds shear stress anisotropy becomes:

$$\Pi_{12(curvature)} = \frac{\mathcal{S}k}{\varepsilon}[[a_{11}C_3 - a_{22}(1-C_2)][1-\xi] + \xi(2 - C_2 + C_3)(a_{11} - a_{22})] \tag{A.6}$$

Which can be compared to Eq. (A.5). The analogy between rotation and curvature is through the second term in Eq. (A.6). In practice, this is dominant over the curvature contribution through the first term. For $\mathcal{S} > 0$ and $\xi > 0$, curvature results in increased rate of production of the Reynolds shear stress anisotropy. The magnitude of shear stress production, however, is decreased because $\overline{uv}$ is negative in parallel shear flows. $\xi < 0$ results in increased magnitude of shear stress production. Hence, curvature is analogous to rotation in that it can either suppress or amplify production of turbulent shear stress. It can be observed that ξ has the same role as $-\Omega^F/\mathcal{S}$ in rotating flows.

A.2. Bifurcation analysis: Combined effects of rotation and curvature

We use the framework developed in Durbin and Pettersson-Reif (2010) for the bifurcation analysis of SMCs and extend it to the combined effects of rotation and curvature making use of the analogy between rotation and curvature developed in Section Appendix A.1.

An explicit solution is sought for Eq. (A.1) with $d_t a_{ij} = 0$ resulting in the following relation for $\varepsilon/\mathcal{S}k$ vs. $\Omega^F/\mathcal{S}$, termed the branch 1 solution:

$$\frac{(1/4)(\varepsilon/\mathcal{S}k)^2_\infty}{g^2(1-\xi)^2(1-C_2-C_3)^2} = \frac{2}{3} + \frac{(4/3 - C_s)}{(1-C_2-C_3)^2 g\mathcal{P}_\mathcal{R}} - 2 \times \frac{(1-C_2+C_3)^2}{(1-C_2-C_3)^2}\mathcal{R}^2 \tag{A.7}$$

where $g = 1/(C_1 - 1 + \mathcal{P}_\mathcal{R})$.

On the branch 2, $\varepsilon/k = 0$. Setting this and rearranging Eq. (A.7) gives

$$(4/3 - C_s)\frac{C_1 - 1 + \mathcal{P}_\mathcal{R}}{\mathcal{P}_\mathcal{R}} = 2(1 - C_2 + C_3)^2\mathcal{R}^2 - \frac{2}{3}(1 - C_2 - C_3)^2 \tag{A.8}$$

which gives $\mathcal{P}_\mathcal{R}$ vs. $\mathcal{R}$ on branch 2. The definition of $\mathcal{R}$ has been generalized for the case with both rotation and curvature as:

$$\mathcal{R}^2 \equiv \left(\frac{\Omega(1+\xi)}{\mathcal{S}(1-\xi)} + 2\frac{(2 - C_2 + C_3)\Omega^F}{(1 - C_2 + C_3)\mathcal{S}(1-\xi)} - 2\frac{\xi}{(1 - C_2 + C_3)(1-\xi)}\right)^2 \tag{A.9}$$

with $\Omega = -\partial_y U$ and $\mathcal{S} = \partial_y U$ in homogeneous shear flow.

The bifurcation diagrams plotted in Fig. A.15 for rotating homogeneous shear flow and curved homogeneous shear flow are special cases in Eq. (A.9) with $\xi = 0$ and $\Omega^F/\mathcal{S} = 0$ respectively. In Fig. A.16, we compare the effect of neglecting the convective transport (corresponds to the last term in Eq. (A.9)), while taking the equilibrium approximation. The plot indicates that turbulence stabilization occurs much earlier when the convective transport term is included, underscoring the importance of this term. The bifurcation surface for the combined effects of rotation and curvature is plotted in Fig. A.16. It can be observed that when $\Omega^F/\mathcal{S} > -0.15$, there is a second ξ-bifurcation point. It means that the linearized SSG model predicts stabilization even for concave curvatures in non-rotating flows which is unphysical.

References

Arolla, S.K., Durbin, P.A., 2012a. Incorporating Rotation and Curvature Effects in Scalar Eddy Viscosity Closures. AIAA Paper 2012-3283.

Arolla, S.K., Durbin, P.A., in preparation. On the Numerical Implementation of a Rotation/Curvature Correction for Turulence Models in a Finite Volume CFD code. Prog Comput Fluid Dy.

Barlow, R.S., Johnston, J.P., 1988. Structure of a turbulent boundary layer on a concave surface. J. Fluid Mech. 191, 137–176.

Barri, M., Andersson, H.I., 2010. Turbulent flow over a backward-facing step. Part 1. Effects of anti-cyclonic system rotation. J. Fluid Mech. 665, 382–417.

Boysan, F., Ewan, B.C., Swithenbank, J., Ayers, W.H., 1983. Experimental and theoretical studies of cyclone separator aerodynamics. IChemE Symposium Series No, 69, pp. 305–320.

Cazalbou, J., Chassaing, P., Dufour, G., Carbonneau, X., 2005. Two-equation modeling of turbulent rotating flows. Phys. Fluids 17, 1–14.

Dhakal, P.T., Walters, K.D., 2011. A three-equation variant of the SST $k-\omega$ model sensitized to rotation and curvature effects. J. Fluids Eng., 133.

Duraisamy, K., Iaccarino, G., 2005. Curvature correction and application of the $v^2 - f$ turbulence model to tip vortex flows. In: Annual Research Briefs. Center for Turbulence Research, Stanford University.

Durbin, P.A., 1993. A Reynolds stress model for near-wall turbulence. J. Fluid Mech. 249, 465–498.

Durbin, P.A., 2011. Review: adapting scalar turbulence closure models for complex turbulent flows. J. Fluids Eng..

Durbin, P.A., Medic, G., 2007. Fluid Dynamics with a Computational Persepctive. Cambridge University Press, New York.

Durbin, P.A., Pettersson-Reif, B.A., 1999. On algebraic second moment models. Flow, Turbul. Combust. 63, 23–37.

Durbin, P.A., Pettersson-Reif, B.A., 2010. Statistical Theory and Modeling for Turbulent Flows, second ed. John Wiley and Sons, New York.

Gatski, T.B., Jongen, T., 2000. Nonlinear eddy viscosity and algebraic stress models for solving complex turbulent flows. Prog. Aerosp. Sci. 36, 655–682.

Gillis, J., Johnston, J.P., Kays, W.M., Moffat, R.J., 1980. Turbulent Boundary Layer on a Convex Curved Surface. Ph.D. Thesis. Dept. Mech. Eng., Stanford University.

Girimaji, S., 1997. A Galilean invariant explicit algebraic Reynolds stress model for turbulent curved flows. Phys. Fluids 9 (4).

Grundestam, O., Wallin, S., Johansson, A.V., 2008. Direct numerical simulations of rotating turbulent channel flow. J. Fluid Mech. 598, 177–199.

Hellsten, A., 1998. Some Improvements in Menter's $k-\omega$ SST Turbulence Model. AIAA Paper 1998-2554.

Holloway, A.G.L., Tavoularis, S., 1989. The Effects of Curvature on Sheared Turbulence. Ph.D. Thesis. University of Ottawa.

Howard, J.H.G., Patankar, S.V., Bordynuik, R.M., 1980. Flow prediction in rotating ducts using coriolis-modified turbulence models. J. Fluids Eng. 102, 456–461.

Johnson, P.L., Johnston, J.P., 1989. The Effects of Grid Generated Turbulence on a Flat and Concave Turbulent Boundary Layers. Ph.D. Thesis. Dept. Mech. Eng., Stanford University.

Johnston, J.P., Halleen, R.M., Lezius, D.K., 1972. Effects of spanwise rotation on the structure of two-dimensional fully turbulent channel flow. J. Fluid Mech. 56, 533–557.

Kalitzin, G., Medic, G., Iaccarino, G., Durbin, P.A., 2005. Near-wall behavior of RANS turbulence models and implications for near wall functions. J. Comput. Phys. 204, 265–291.

Khodak, A., Hirsch, C., 1996. Second order nonlinear models with explicit effect of curvature and rotation. In: Proc. 3rd ECCOMAS Computational Fluid Dynamics Conf., Paris. pp. 690–696.

Kristoffersen, R., Andersson, H.I., 1993. Direct simulations of low-Reynolds-number turbulent-flow in a rotating channel. J. Fluid Mech. 256, 163–197.

Laskowski, G.M., Durbin, P.A., 2007. Direct numerical simulations of turbulent flow through a stationary and rotating infinite serpentine passage. Phys. Fluids, 18.

Lund, T.M., Moin, P., 1996. Large-eddy simulation of a concave wall boundary layer. Int. J. Heat Fluid Flow 17, 290–295.

Menter, F.R., 1992. Improved two-equation $k-\omega$ Turbulence Models for Aerodynamics Flows. Tech. Rep. TM-193975, NASA.

Menter, F.R., 1993. Zonal Two Equation $k-\omega$ Turbulence Models for Aerodynamic Flows. AIAA Paper 1993-2906.

Pettersson-Reif, B.A., Durbin, P.A., Ooi, A., 1999. Modeling rotational effects in eddy-viscosity closures. Int. J. Heat Fluid Flow 20, 563–573.

Simon, T.W., Moffat, R.J., Johnston, J.P., Kays, W.M., 1982. Turbulent Boundary Layer Heat Transfer Experiments: Curvature Effects Including Introduction and Recovery. Tech. Rep. CR 3510, NASA.

Slack, M.D., Prasad, R.O., Bakker, A., Boysan, F., 2000. Advances in cyclone modeling using unstructured grids. Trans. IChemE, Part A, 78.

Smirnov, P.E., Menter, F.R., 2009. Sensitization of the SST turbulence model to rotation and curvature by applying the spalart–shur correction term. J. Turbomach., 131.

Spalart, P.R., Shur, M.L., 1997. On the sensitization of turbulence models to rotation and curvature. Aerosp. Sci. Technol. 1, 297–302.

Speziale, C.G., MacGiollaMhuiris, N., 1989. On the prediction of equilibrium states in homogeneous turbulence. J. Fluid Mech. 209, 591–615.